

High Contrast Vacuum Nuller Testbed (VNT) Contrast, Performance and Null Control

Richard G. Lyon^{*a}, Mark Clampin^a, Peter Petrone^b,
Udayan Mallik^a, Timothy Madison^a, Matthew R. Bolcar^a
^aNASA/Goddard Space Flight Center, Greenbelt, MD 20771;
^bSigma Space, Lanham MD

ABSTRACT

Herein we report on our Visible Nulling Coronagraph high-contrast result of 10^9 contrast averaged over a focal plane region extending from $1 - 4 \lambda/D$ with the Vacuum Nuller Testbed (VNT) in a vibration isolated vacuum chamber. The VNC is a hybrid interferometric/coronagraphic approach for exoplanet science. It operates with high Lyot stop efficiency for filled, segmented and sparse or diluted-aperture telescopes, thereby spanning the range of potential future NASA flight telescopes. NASA/Goddard Space Flight Center (GSFC) has a well-established effort to develop the VNC and its technologies, and has developed an incremental sequence of VNC testbeds to advance this approach and its enabling technologies. These testbeds have enabled advancement of high-contrast, visible light, nulling interferometry to unprecedented levels. The VNC is based on a modified Mach-Zehnder nulling interferometer, with a "W" configuration to accommodate a hex-packed MEMS based deformable mirror, a coherent fiber bundle and achromatic phase shifters. We give an overview of the VNT and discuss the high-contrast laboratory results, the optical configuration, critical technologies and null sensing and control.

Keywords: Exosolar planets, high contrast imaging, visible nulling coronagraph, visible nulling interferometer, coronagraph, wavefront sensing, wavefront control, null control, nulling interferometry

1. INTRODUCTION

The visible nulling coronagraph (VNC) is an approach to the challenge of direct detection and characterization of exosolar planets. It is currently the only known internal coronagraph approach that works with filled, segmented and sparse or dilute aperture telescope systems [1] with the only modification for different architecture being the shape of the Lyot stop. Space telescope system concepts that are based on this approach include: the Extrasolar Planetary Imaging Coronagraph [2,3,4] (EPIC), Diluted Aperture Visible Nulling Coronagraphic Imager [5] (DAViNCI), and, the Advanced Technology for Large Aperture Space Telescope [6] (ATLAST). These were three separate NASA Astrophysics Strategic Mission Concept studies, each of which assessed the feasibility of using a VNC [7,8,9,10] as their prime instrument for exoplanet detection and characterization. The three studies spanned the space of possible aperture configurations of filled, segmented, and diluted/sparse aperture configurations for which the VNC is well suited. The VNC was originally designed and developed for EPIC, but new VNC implementations have been put forth for both ATLAST and DAViNCI [8]. It also lends itself to balloon borne payloads [15] and for ground instruments in both visible and near-infrared (NIR) light.

The VNC would enable such flight missions to provide insights into the physical nature of a variety of planets in other solar systems complimenting radial velocity (RV) and astrometric planet searches. It would detect and characterize the atmospheres of planets identified by radial velocity surveys, determine orbital inclinations and masses, characterize the planetary atmospheres, and observe the inner spatial structure and colors of inner debris disks [13].

The VNC approach is shown in **Figure-1** and it consists of a modified Mach-Zehnder interferometer with two output ports. It is modified since it has three reflections in each arm, as opposed to two in a conventional Mach-Zehnder. One of the reflections is a specialized deformable mirror known as a multiple mirror array (MMA) that consists of MEMS based hexagonally shaped and hexagonally packed segments [11]. Each segment is articulated in 3 controlled degrees-of-freedom for piston, tip and tilt. The VNC spatially splits the beam into two separate optical paths at the first beamsplitter (BS) and recombines them with a π phase shift at the second BS. If both beams in each path are identical in amplitude, phase, polarization and wavelength, then nulling occurs due to destructive interference, and no light would exit the output port labeled as science (SCI).

, Tlej ctf\ N{qpB pcuc\ qx=j qpg'523/4: 8/6524"

"

Conversely, all of the light would exit the output channel labeled pupil wavefront control (Pupil-WFC). Variations in the optical path difference, between the two-interferometer arms, induced by wavefront (phase), amplitude, polarization, and spectral effects cause light to leak through to the SCI output. These variations occur both spatially (laterally across the beam), and their temporal variations are due to thermal drift, vibration and pointing jitter. The net effect of this light leakage is to lower the contrast of the planet with respect to the star. The VNC is a symmetric interferometer in that a tip or tilt of the input beam walks the light in the recombined output beams in the same direction, e.g. a Michelson would walk the light in two opposite directions resulting in twin images of the planet.

The VNC is implemented as a coronagraph by introducing an additional phase shift as a function of field angle on the sky. If the path length differences are set such that the phase difference is π on-axis then all on-axis starlight would exit the Pupil WFC. A phase shift of zero, off-axis at the location of the planet, would pass all the planetary light to the science channel. The contrast is defined to be the ratio of the two. The field dependent phase shift can be introduced a number of ways, e.g. laterally shearing one beam in one arm of the interferometer relative to the other arm. A shear of 25% of the beam diameter results in a piston-like phase difference off-axis that grows linearly with field angle and such that the sine of the piston reaches its 1st maxima at $2\lambda/D$ in angle on the sky. This is generally taken as its inner working angle (IWA), where λ is the wavelength and D is the aperture diameter (or longest baseline for a sparse/dilute system). Other approaches to introducing the field dependent phase shift are to shape the surfaces of the two flat optics in one arm of the interferometer that are at non-pupil images of the entrance aperture (labeled as non-Pupil "W" optics in **Figure-1**). Since these optics are not at a pupil, the beam walks across these optics with increasing field angle, and the surface shapes are tailored such that the induced phase shift is π on-axis and smoothly changes to zero at the IWA. Use of this approach mitigates the need to shear, thereby removing a mechanism for shifting the beams. Additionally there is no region where the recombined beams are not overlaid. This effectively enables a simple, high efficiency Lyot stop, since it contains the entire pupil image, not just the overlaid sheared region.

The basic principle of the VNC has been adequately described elsewhere and the mathematical model of how it operates is well understood, see for example, Lyon et. al, 2006, 2008 and the references therein.

Past work has concentrated on proof of principle and we have subsequently demonstrated nulling [9] and high contrast imaging [14] and the ongoing phase of the VNT efforts are concentrated on quantification of its performance and advancing and refining its control approach. The next phase is to push towards broadband visible nulling approaching the 10^{10} contrast level.

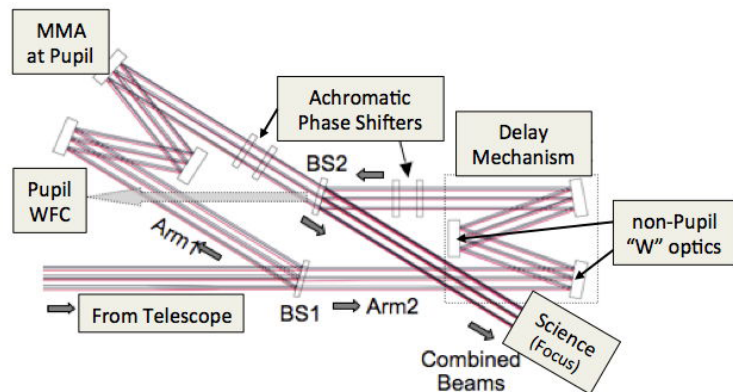


Figure 1 – Optical Layout of Visible Nulling Coronagraph. Photon flux is conserved across both output channels: (1) Pupil wavefront control and (2) in-focus Science channel; independent of the state of the VNC, thereby setting a fixed control bandwidth for a given target star, enabling rapid and precise high contrast null control to compensate for differential path length errors.

2. VACUUM NULLER TESTBED

The VNT has been developed to meet the contrast milestones of 10^8 and 10^9 , both narrowband, and at an IWA of $2\lambda/D$. Additionally we expect to achieve future milestones that are both broader band and higher in contrast. The approach taken is to treat it as a successive process of evaluation, whereby we evaluate the critical technologies, at first separately, then after integration into the testbed and traceable to the science enabling flight requirements of contrast, IWA, spectral bandpass and system stability. The critical technologies include: (i) multiple mirror array (MMA), (ii) spatial filter array

(SFA), (iii) achromatic phase shifters (APS), (iv) null control, and (v) photon counting detectors and all are at various stages of development with further development expected to occur.

2.1 Description of the Visible Nulling Testbed

A top-down photograph of the VNT in its current state is shown in **Figure-2**. The VNT resides on a 24" x 36" optical table. Light enters from a super continuum source outside the vacuum chamber through a single mode fiber at the bottom center of **Figure-2**. Light exits the single mode optical fiber as approximately as an expanding Gaussian beam into a tubular light trap with black absorbing material. Light can only exit at the left face of the light trap through a 2" apochromatic collimating lens. The lens is stopped down by a circular, black coated, custom metal aperture, to let light

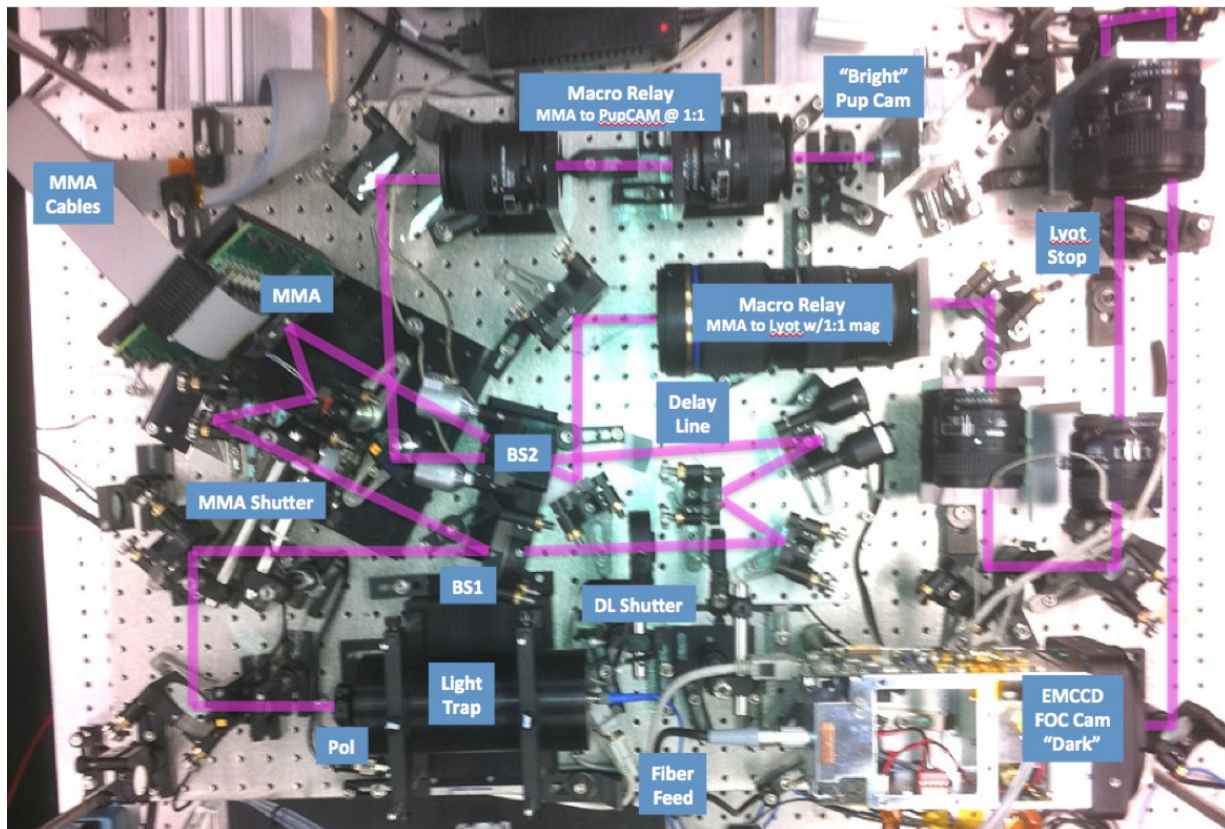


Figure 2 – Photograph of Visible Nulling Testbed (VNT). Optical paths are illustrated in purple. The VNT is on a 36 x 24-inch, 5 inch thick stainless steel platform that can be hoisted into a vacuum tank. Light enters from a source module at bottom center at 'Fiber Feed'. The source module consists of a supercontinuum source with neutral density filters and spectral filters. Light from the source is spatially and spectrally filtered prior to entering the VNT.

exit only over the central 1.6 cm aperture diameter. This effectively forms the aperture stop for the system and allows only $\sim 1/3$ of the central diameter of the Gaussian beam to exit insuring a nearly perfect wavefront and amplitude quality, i.e. a high order approximation to a plane wave. A linear polarizer is within the exit port of the light trap with the polarization axis set such that the E-field vector is perpendicular to the plane of **Figure-2**. This is to insure initially that all reflective optics sees transverse electric (TE) mode fields to minimize polarization cross-leakage. The symmetry of the nuller makes it insensitive to the polarization state of the input field in principle, however differences in coatings, and reflection angles, introduce polarization mismatches. There are two polarizers within the interferometer, one per arm, and two more polarizers, one in front of the two output cameras. Nominally these are all set to the same angle by using a Glan-Thompson prism, and then the two polarizers within the interferometer are rotated such that the light output separately from each arm is matched to within 0.1%. The shutters in each arm are used to accomplish this, as well as monitor the polarization, perform background subtraction and to calculate the contrast. This can be better understood by Equation-1. An output image of the aperture stop on the cameras would yield an image of the form:

$$I(\vec{r}) = I_1(\vec{r}) + I_2(\vec{r}) \pm 2\sqrt{I_1(\vec{r})I_2(\vec{r})} \cos[\phi(\vec{r})] + B(\vec{r}) + \eta(\vec{r}) \quad [1]$$

where I_1 and I_2 represent the beams in the two interferometer arms respectively, ϕ represents the difference in phase errors in traversing the interferometer, B is the background and incoherent stray light, η is noise and $\vec{r} = (x, y)$ is the pupil plane coordinate. The \pm is for the bright and dark output channels respectively. Shutting both shutters estimates B and averaging many frames reduces the standard error on B as σ/\sqrt{N} where σ is the noise standard deviation and N is the number of frames. In practice N is set to reduce the standard error to less than 0.01 counts of the detector. Opening shutter-1 gives $I_1 + B$ and closing shutter-1 and opening shutter-2 gives $I_2 + B$ and subtracting off the background from each allows for both to be estimated *in-situ* to compensate for source, background, and camera drift. Thus the shutters function as choppers. If instead of operating in the pupil plane, we operate from the focal plane for the dark channel then the shutters still give the I_1 and I_2 terms and the sum of these terms gives the counts without any nulling, i.e. with constructive interference. This yields the numerator for the contrast ratio.

After the light trap is an optical relay that images the aperture stop onto the MMA and its counterpart in the other arm of the interferometer, i.e. a real pupil image. There are two custom matched beamsplitters made of high-grade fused silica with dielectric coatings, the first is used to split the beam and the 2nd to recombine. The 1st beamsplitter has its coated side facing the incident light while the 2nd beamsplitter is flipped with the coating side facing in the opposite direction. At the 1st beamsplitter the light is split into a reflective path towards the upper left and a transmissive path towards the right. The transmissive path reflects off three flat optics that are mounted in a “W” configuration. The “W” is aligned such that the input and output beams are parallel and is built and aligned as a separate rigid assembly. This assembly is mounted on a two stage (coarse and fine), 1 degree-of-freedom (DOF) translation stage known as the delay line mechanism. This mechanism is used to change the overall path length in the transmissive arm relative to the reflective arm. The coarse mechanical mechanism is used only at the outset to acquire, and center, the white light fringe – white light since a broader spectral filter is initially used to insure we locate the central fringe. This alignment is subsequently refined by the fine (piezo) such that the path length differs by < 20 nm at the outset of the closed-loop control. Initially we attempted to actively control the piezo during closed-loop operations but found that using the MMA in closed-loop yields a faster, more precise, and stable control of the path length difference.

Following this step the bright channel pupil plane image is used to walk in and indirectly control the wavefront errors by sensing only detector counts, and their variance, over the region of each segment in the pupil image. A metric is used as a weighted sum of the mean counts per segment and variance per segment. Conceptually one would want to drive the pupil image bright which yields a dark focal plane image, however it is less sensitive to drive it bright than to drive it dark, i.e. if one averages the light per MMA segment over each segment and drives the piston, tip and tilt control for each segment to minimize its pupil brightness, then small deviations in the wavefront cause large changes in the averaged light per segment. In practice this camera is limited to a dynamic range of $\sim 10^4$ and this directly limits the sensing and control of the pupil plane null depth. Note that in the pupil domain each segment is independent of each other (control law is diagonal), and thus the algorithm is trivially parallelizable for optimum speed. Once a dark pupil plane is achieved and held stable, the segments are pistoned to realize a phase shift, making them appear bright and the dark channels jumps to a darker state by approximately 4 orders of magnitude. Fine control is now handed off to the dark focal plane. The basic control in the dark focal plane is accomplished by identifying a region, or patch, of the image that we desire to drive dark and iterating the segment motions with predictive/corrective feedback, to minimize the light in this region.

In practice the choppers are used periodically to subtract off background and a temporal integrator is used to insure that enough light is available to sense and control within the dark hole - as the hole gets successively darker more frames must be integrated to yield this condition. Additionally low order wavefront modes were found to drift slowly and these are fit to a polynomial in time and the prediction extrapolated to the next control step with the algorithm working to minimize the observed difference between the predicted and observed darkness state. If an out of spec condition occurs control can be relegated back to the pupil control. Additionally control can use a weighted form of both the dark and bright channel outputs. During nominal operation there is no wavefront sensing in the classical sense, i.e. only detector counts are collected and piston, tip, tilt error signals are generated to minimize detector counts within the defined focal plane region, i.e. dark hole. Thus the sensing and control does not care whether the errors are from amplitude or phase it

only minimizes the detector count which implicitly works to minimize both amplitude and wavefront errors without the need to separate them. This makes the control approach simple and easier to implement. The control aspects of the VNC are very robust and repeatable but the mathematical details will not be described herein as it would take us far from this descriptive overview.

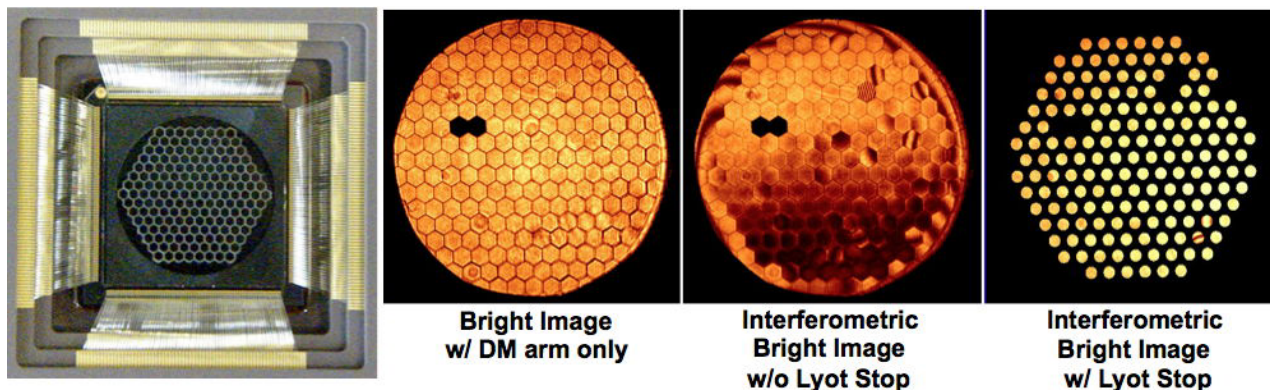


Figure 3 – *Far left*: Photo of an IRIS-AO Multiple Mirror Array (MMA). 169 segments of which 163 are active (outermost 6 inactive). Each segment is ~700 microns point-to-point, gaps are 8 – 10 microns. Full width of active area is ~8.5 mm. Segments are 50-um thick single crystal Si overcoated with protected Al, each moves in 3-DOF. Surface is photographed reflecting black cardboard to accent segment gap locations. *Left of center*: Image on the pupil-WFC camera with only the VNC arm containing the MMA open and Lyot stop open – no interference fringes are present. *Right of center*: Image on the pupil-WFC camera with both VNC arms open and Lyot stop open after MMA flats file has been applied – interference fringes are present around outer edge and a < 1 cycle per aperture (cpa) fringe is evident from top to bottom. *Far right*: Image on the pupil-WFC camera with both VNC arms open and Lyot stop closed – 1 cpa interference fringe has been compensated for with MMA control and MMA segments are Lyot masked to restrict edge effects and to remove the 5 bad segments.

2.2 Test Configuration

The VNT resides with a vacuum chamber and the vacuum chamber rests on the top surface of a 1-Hz air isolation table. The source module is external to the vacuum chamber and is contained within a removable black box. The self-contained source module mitigates air turbulence, damps acoustic vibration, and removes unwanted stray light and alleviates safety concerns relative to the super-continuum source contained within it. The optical output of the source module is fiber coupled through the bulkhead of the vacuum chamber. The MMA control electronics, and delay line electronics are external to the vacuum chamber and analog and digital lines pass through the bulkhead to the devices. The VNC rests on decoupled shelf within the vacuum chamber and it is decoupled in the sense that it rests on passive isolators within the chamber. The chamber itself rests on passive isolators between the tabletop and the chamber. A water-based chiller system removes excess heat from the EMCCD camera head and radiative and conductive heat straps are used to remove heat from the hot power chips on the EMCCD circuit boards. All results reported on here in are using this configuration.

2.3 Description of the Multiple Mirror Array

The reflective arm of the nuller also traverses a “W” configuration towards the upper left. The third optic in the reflective optical path is the microelectromechanical (MEMS) deformable mirror with a hexagonal packed segmented face sheet known as a multiple mirror array (MMA) as shown in **Figure-3** and described in references [11, 12]. Each of the MMA segments are individually actuated with electrostatic flexure actuators such that each of the segments moves as a rigid body in piston, tip and tilt (3-DOF). The MMAs function is to minimize the wavefront difference between the two arms of the nuller.

Both the transmissive and reflective arms of the nuller are combined at the 2nd beamsplitter and yield two output beams known as the bright (pupil-WFC) and dark (science) channels as labeled in **Figure-1**. Only the dark channel is truly symmetric since it sees the coherent sum of a beam that first reflects off beam splitter-1, and subsequently transmits through beam splitter-2 coherently added to the beam which transmits through beam splitter 1 and reflects off beam splitter 2, i.e. $E_D \propto rt + rte^{i\pi} = 0$ where the π phase shift is introduced by the path length difference between the two nuller arms. The bright channel sees a coherent sum of a beam that reflects off both beamsplitters added to a beam that

transmits through both beamsplitters, i.e. $E_B \propto r^2 + t^2$ and is thus more sensitive to imbalance in the reflection and transmission of the two beamsplitters. The bright and dark channels pass through two macro lens groups which for the bright channels relays an image of MMA onto a 16-bit CMOS high frame-rate detector, i.e. a pupil image. The dark channel detector sees a focal plane image on a photon counting cooled E2V camera. All the optics which appear in the non-common path arms of the nuller are high quality flat optics with fused silica substrate and coated with the same broadband coatings except for the MMA and its counterpart in the other arm, both which are coated with protected aluminum from the same coating vendor to balance reflectivities. Additionally the MMA has segment gaps, which are not resident in the other arm of the nuller. The segment gaps introduce Fresnel diffraction effects that are different from the other arm. To correct

this problem a high quality optical relay is placed at the output of the VNC after the 2nd beamsplitter. This relay “sees” both the MMA and its counterpart optic in the opposite arm and images them such they are overlaid in the exit pupil (**Figure-3** two right most images). The aperture of the relay is sufficient to capture the wider angle Fresnel ringing from the

free space propagation of the segment gaps resulting in a high quality pupil image. This re-imaged pupil is labeled as Lyot stop in **Figure-2**; a physical stop is placed at this plane that consists of circular holes laser ablated into titanium foil (**Figure-3** far right) and the foil is coated with highly absorbing black coatings. The holes are 400 microns in diameter while the segments are on a lattice of 613 microns and thus the Lyot stop serves to reduce straylight and to mitigate edge effects, and mask bad segments, on the MMA. The Lyot stop is the exit pupil of the VNC.

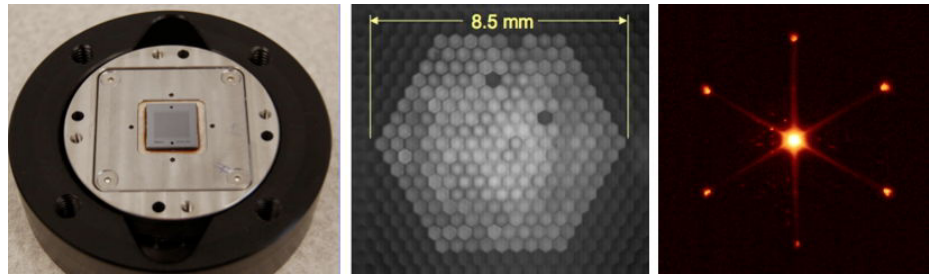


Figure 4: – *Left:* Spatial Filter Array (SFA) with 217 active fibers; shown w/o lenslets but assembled. *Middle* – Image of output side with lenslets in white light showing hex array pattern. *Right* - First focal plane image through SFA, with HeNe laser light, showing the phased array pattern indicative of the requisite spatial coherence.

2.4 Description of the Spatial Filter Array

The spatial filter array (SFA) assembly resides in the recombined dark output channel. Though not shown explicitly in **Figure-2**, it is positioned on a special mount that allows it to be removed and inserted with minimal realignment, and would be placed where the Lyot stop is. Initially the SFA has not yet been used to attain the contrasts reported on herein. It has however been separately tested prior to its integration into the VNT later this summer. The SFA is shown in **Figure-4** and consists of an input lenslet array followed by an array of single mode fibers followed by an output array of lenslets. Each input lenslet is mapped to one fiber and to one output lenslet and each lenslet-fiber-lenslet is optically mapped to one MMA segment, thus each channel of the SFA is mapped to one segment of the MMA (**Figure-4** center). When used passively the SFA cleans up the wavefront errors on the scale of 1 cycle per MMA segment, since these will be spatially filtered by the fiber. When used in conjunction with the tip/tilt control of the MMA the PSF of a single segment can be steered onto the end of the fiber to lower the coupling efficiency into the fiber. Since the MMA is only in one arm of the VNT, it only affects that component of the beam. If the other arm is slightly darker then mis-steering can be used to balance the amplitude between the beams. Thus the MMA in conjunction with the SFA can in principle control both amplitude and wavefront errors simultaneously. This principle will be validated and its performance assessed. **Figure-4** right shows the first observed focal plane image through the SFA, in HeNe laser light. If the separate optical paths of the SFA were spatially incoherent then each optical channel's point spread function (PSF) would add incoherently and each of these PSFs would subtend the region out from the bright center to the first ring of 6 sidelobes as shown in **Figure-4** right. However, a coherently phased sum would collapse down to yield the phased-array PSF with a sharp central core and sidelobes as shown in **Figure-4** right – effectively demonstrating the SFA as a spatially coherent device.

2.5 Overview of Null Control

The overall null control is really a multi-step process that consists of a set of camera, delay-line, and amplitude balancing calibration algorithms, sensing algorithms and delay line and MMA control algorithms. We will not describe herein the mathematical development of the algorithms but do describe the sequence of steps to calibrate and subsequently

successively lower the rms wavefront error, followed by the fine null control to drive a region of the science focal plane as dark as possible and to hold it there in closed loop. The sequence of 6 steps is described below.

The fine null control refers to sensing and controlling the light and driving it dark to maximize the contrast. It is a misnomer to refer to it as wavefront control since there is no attempt to separate wavefront from amplitude errors, nor to directly sense and control wavefront error. It is critical to be able to optimally sense and control the null with enough control bandwidth to first achieve and hold the contrast, and, to do this repeatedly without levying extreme stability tolerances on the testbed, nor on a flight system. The stroke of the MMAs, bit depth of the cameras, vibration, thermal drift, coating imperfections, temporal and spatial sampling, quantization, flat fielding, dark current, noise, stray light, approximations and errors in the algorithms, along with other potential effects, all work to corrupt this process.

A descriptive discussion of this suite of algorithms is given in [14] and a control sequence description is as follows:

1. *Balancing the DC field amplitudes:* A series of N dark channel images are collected and averaged with one shutter open and the other closed and then again with the shutters reversed, and then with both shutters closed. Each of the 3 sets of N images are averaged and standard error frames are calculated, and the mean background frames are subtracted off the pair of average images with the shutters interlaced. When the difference in the integral counts is less than 0.01 counts +/- 0.001 counts the two arms of the interferometer are balanced. If not then polarizers are rotated until this condition is met. This balancing is independent of the state of the MMA.
2. *Grabbing the handles to the devices:* MMA, pupil-WFC camera, focal plane camera and delay line. Grabbing the handle refers to accessing the MMA within the software, and the MMA at this point has zero voltage applied to each actuator and is in a state with multiple tip/tilt fringes and piston delays between the segments.
3. *Flattening the MMA:* This consists of loading a look-up table known as a "flats file" that contained the last state from the previous MMA flattening effort. The flattening effort consists of using N-bucket/Hilbert transform type algorithms to flatten the MMA relative to the other arm of the interferometer.
4. *Removing global low-order WFE:* Over the course of several days, the flats file becomes less viable due to global low order wavefront drifts of the entire pupil image, i.e. not per segment, as shown in the image right of center image of **Figure-3**. Removing the low-order WFE is accomplished by using a look up table of numerical fits of the actuator motions to global piston, tip, tilt, astigmatism, power, coma, trefoil and spherical aberration and dithering these terms to minimize a metric to achieve both the flattest wavefront and such that the piston dithers drive the pupil image as dark as possible. After this step the rms WFE difference between the two interferometer arms is <20 nm rms.
5. *Inverting the phase:* The individual pistons on each segment is shifted to impart a π phase shift thereby driving the pupil-WFC image uniformly bright and simultaneously driving the in-focus science image dark by approximately 4-orders of magnitude.
6. *Fine Null Control:* A [0,1] mask is loaded from disk containing the region of the focal plane to drive dark, 1 for a valid pixel and zero for an irrelevant pixel. Over this region a set of metrics are calculated that consist of average counts, variance of counts, and rejection outlier average and variance of the counts. The rejection outlier algorithm is used to fine-tune the location of the mask and to identify pixels and/or regions that appear more difficult to control. A modal control algorithm is then employed with a subset of discrete and orthogonal basis vectors, or modes, with the most sensitivity, or gain, for the region of control. The algorithm proceeds by using only those low order modes and iterating until these modes are changing by only small amounts and then adding in higher modes and continuing.

In practice we found that 10^9 contrast required ~250 control modes, but that 10^8 could be achieved with as few as ~70 control modes. The fine null control is operated in closed-loop at 40 Hz, i.e. 40 camera frames per second (fps) from both the bright pupil-WFC camera and 40 fps from the dark focal plane camera. An exponential integrator is used (single pole filter) to allow control of temporal frequencies up to 4 Hz (half power point) and the first N mode changes are fit to a polynomial to extrapolate to the next time point in the control sequence. The control metric, with feedback to the MMA, acts to minimize the rms difference between the predicted and corrected dark-hole metric value acts like an ARMA type filter or a simple Kalman filter.

2.6 High Contrast Results

The VNT was used to achieve high contrast imaging consisting of 4 data collection events (DCE) spanning the time period of June 9th, 2012. Each DCE consisted of the sequence steps 2 through 6 described in section-2.5. Step-1 was performed prior to DCE-1 since the amplitude re-balancing changes slowly, i.e. on the times scale of weeks to months.

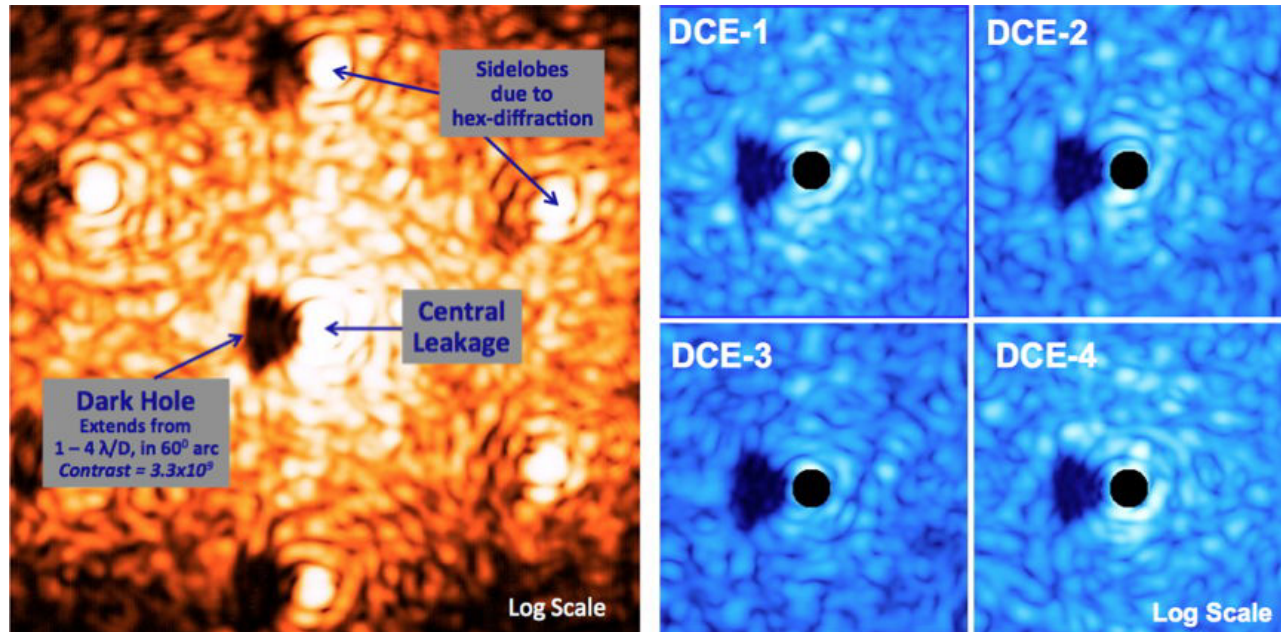


Figure-5: *Left* – Annotated image (512 x 512) of average of last 3,800 frames DCE-1 (06/09/2012) showing the science focal plane on a log-scale. The central leakage is 10^4 darker than without any nulling and the region labeled ‘dark hole’ is 10^5 times darker yielding an overall contrast of $>10^9$ when averaged over the dark-hole region. The dark-hole region extends from $1 - 4 \lambda/D$ and in a 60 degree arc left of center. Image plate scale is 16.8 pixels per λ/D and the images shows a full FOV of $30.5 \times 30.5 \lambda/D$. *Right* - Central region of the average of last 3,800 frames for each of the 4 DCE’s. Each of which is after steps 2 – 6 of the control sequence and separately resulted in 4 separate realizations of average contrasts exceeding 10^9 .

Step-7 consisted of 50,000 images per DCE and where the contrast results are tabulated on the last 3,800 images. Approximately 30,000 steps are required to bring the VNC to a contrast of 10^9 and the last 3,800 images are the most stable and yield the highest measured contrasts with a nulling interferometer to date. Each of the 3,800 frames are separated in time by 0.25 seconds, i.e. 4 Hz of 4 frames per second, and spanning 950 seconds.

Figure-5 left is an annotated image of the average of the last 3,800 camera frames of DCE-1 showing the science focal plane on a log-scale. The labeled central leakage is 10^4 darker than without nulling and the region labeled ‘dark-hole’ is 10^5 times darker yielding an overall contrast of $>10^9$ when averaged over the dark-hole region. The dark-hole region extends from $1 - 4 \lambda/D$ and in a 60-degree arc left of the image center. Image plate scale is 16.8 pixels per λ/D and the 512 x 512 image shows a full FOV of $30.5 \times 30.5 \lambda/D$. The right 4 frames of **Figure-5** show the central regions for all 4 DCEs and each of the 4 images is an average of the last 3,800 frames for each of the 50,000 frames DCE’s. Each DCE consists of steps 2 – 6 of the control sequence and separately resulted in 4 separate realizations of average contrasts exceeding 10^9 .

The source is super-continuum broadband source spectrally filter with a spectral filter centered at 633 nm with a full-width-half-maximum of 1.2 nm giving a high spectral resolution of 528. The reported on contrasts are narrowband, however, they are not a monochromatic result.

2.7 Null Control Stability

Each dark-hole region consists of 1,672 dark camera pixels. 1,672 separate time series are constructed each with 3,800 times samples at 0.25 seconds (4 frames per second) and each time series is separately Fast Fourier Transformed (FFT), modulus squared, to estimate periodograms of each times series. The average of the set of 1,672 periodograms is an estimator of the power spectral density (PSD). The FFT has the property that the frequency sampling is $1/T$ where T is the total time length of time series and herein $T = 3,800 \times 0.25$ seconds = 950 seconds, thus the frequency sampling of the PSD are ~ 0.001 Hz and extends from 0 Hz to 2 Hz (single sided PSD).

Figure-6 plots estimates of the open-loop and closed-loop PSDs, where open-loop is with the fine null control not operating and closed-loop is with it operating. The units of the PSD(f) are camera counts squared per frequency sample such that the integral of PSD(f) from zero to infinity is the expected value of the variance, in detector counts squared, of a given time series. The value of the PSD at a given frequency is the mean square value of a random harmonic at that frequency. There is a clear drift term at ~ 0.004 Hz, or approximately 250 second period, and this is believed due to a slow thermal drift which causes a slowly varying tilt fringe visible in the pupil-WFC camera images – temperature sensors are being installed within the chamber to assess this, however the fine control tracks and removes this drift as seen from the closed-loop PSD. The open-loop PSD transitions to a noise floor that is approximately white noise at greater than 0.2 Hz, or periods of < 5 seconds. The 4 Hz control frequency is 20x faster than the highest frequency drift within the tank and is clearly adequate to achieve and hold 10^9 contrasts. The control is not yet ideal since the closed-loop PSD does not have a purely white noise signature but shows a slowly increasing PSD at low frequencies. It is expected that this will be resolved via better tuning of the control system and better form of integrator than a single pole filter to whiten the closed-loop PSD.

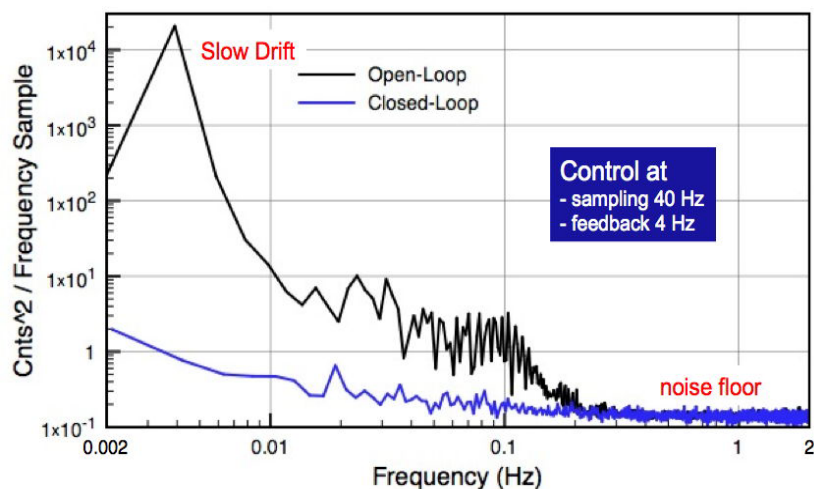


Figure-6: Left –Power Spectral Densities of Open- and Closed-Loop Fine Null Control. A slow drift term, likely thermal, is evident at 0.004 Hz (~ 250 second period). The PSDs transition to white-noise beyond 0.2 Hz.

3. SUMMARY

The direct detection and characterization of exosolar planets, and dust and debris disks, is a crucial step in the search for habitable planets with liquid water, and potentially life, and addresses the NASA *Search for the Origins of Life* theme. Towards that end we have developed the visible nulling coronagraph approach to high-contrast imaging, advanced the necessary technologies at both the component level and at the instrument level and have demonstrated the necessary contrast at inner working angles, in the laboratory, required to detect and characterize dust/debris disks and exosolar Jovian planets in narrowband light. We have reported our high-contrast result of 10^9 contrast averaged over inner working angles from $1 - 4 \lambda/D$ in narrowband light.

The next step is to increase the spectral bandpass from 1.2 nm FWHM to 40 nm FWHM. This will be accomplished by the use of achromatic phase shifters [16] that equalize the optical phase difference to π within the 40 nm spectral bandpass for both polarization states and to demonstrate broader band high-contrast imaging in both polarization states simultaneously.

The VNC approach spans all future flight telescope architectures including filled (both on- and off-axis), segmented and interferometric/sparse aperture telescope systems. Additionally it makes use of all the available output photons for null control since the flux from the target star is conserved from the bright and dark output channels of the VNC. This conservation law yields a robust null control approach that is independent of the state of instrument and its control temporal bandwidth depends only on the brightness of the target star. It does not levy beyond state of the art stability requirements on the telescope since the telescope must be stable only over each integration window for null control.

REFERENCES

- [1] R. G. Lyon, M. Clampin, R. W. Woodruff, G. Vasudevan, P. Thompson, A. Chen, P. Petrone, A. Booth, T. Madison, M. Bolcar, M. C. Noecker, S. Kendrick, G. Melnick, V. Tolls, "Visible Nulling Coronagraphy Testbed Development for Exoplanet Detection", Proceedings of SPIE 7731, San Diego CA (2010)
- [2] M. Clampin, R. G. Lyon, G. Melnick, P. Nisenson, R. A. Woodruff, M. Harwit, D.Y. Gezari, L. Petro, H. Ford, R. Mauk, H. Smith, "The Extra-solar Planetary Imaging Coronagraph", Proceedings of SPIE 5487, Glasgow Scotland, June 21 – 25 (2004).
- [3] M. Clampin, G. Melnick, R. Lyon, S. Kenyon, D. Sasselov, V. Tolls, H. Ford, D. Golimowski, L. Petro, G. Hartig, W. Sparks, G. Illingworth, D. Lin, S. Seager, A. Weinberger, M. Harwit, M. Marley, J. Schneider, M. Shao, M. Levine, J. Ge, R. Woodruff, "Extrasolar Planetary Imaging Coronagraph (EPIC)", Proceedings of SPIE 6265, Orlando FL, May (2006).
- [4] M. Clampin, R. G. Lyon, G. Melnick, V. Tolls, M. Shao, M. Levine, R. A. Woodruff, G. Vasudevan, S. Kendrick, "The Extra-solar Planetary Imaging Coronagraph", Mission for Exoplanets Workshop, Pasadena CA, April 21-23, (2009).
- [5] Shao, M., Bairstow, S. H., Deems, E., Fletcher, L., Levine, B., Orton, G., Vasisht, G., Wayne, L., Zhao, F., Clampin, M., Lyon, R., Guyon, O., Lane, B., Havey, K., Wynn, J. Samuele, R., Vasudevan, G., Woodruff, R., Tolls, V. Malbet, F., Leger, A., "A Mission Concept Study of a Dilute Aperture Visible Nulling Coronagraph Imager (DAVINCI) for the Detection and Spectroscopy of Exo-planets," BAAS #214, (2009).
- [6] Postman, M., "The Science Cases for an Advanced Technology Large-Aperture Space Telescope (ATLAST)," BAAS #215, (2010).
- [7] R. G. Lyon, M. Clampin, R. Woodruff, G. Vasudevan, M. Shao, M. Levine, G. Melnick, V. Tolls, P. Petrone, P. Dogoda, J. Duval, J. Ge, "Visible Nulling Coronagraphy for Exo-Planetary Detection and Characterization", IAU Colloquium 200, Direct Imaging of Exoplanets: Science and Technology, Villefranche-sur-Mer, France, (2006).
- [8] R. G. Lyon, M. Clampin, G. Melnick, V. Tolls, R. Woodruff, G. Vasudevan, "Extrasolar Planetary Imaging Coronagraph (EPIC): Visible Nulling Coronagraph Testbed Results", Proceedings of SPIE 7010, Marseille Fr, (2008).
- [9] R. A. Woodruff, M. Shao, B. Martin Levine, R. Lyon, G. Vasudevan, J. Acu, K. Havey, J. Wynn, "Optical Design of Dilute Aperture Visible Nulling Coronagraph Imager," Proc of SPIE 7731, (2010).
- [10] R. G. Lyon, M. Clampin, R. Woodruff, G. Vasudevan, P. Thompson, P. Petrone, T. Madison, M. Rizzo, G. Melnick, V. Tolls, "Visible Nulling Coronagraph Testbed Results," Proc of SPIE 7440 (2009).
- [11] M. A. Helmbrecht, T. Juneau, M. Hart, and N. Doble, "Performance of a High-Stroke, Segmented MEMS Deformable-Mirror Technology," Invited Presentation, Proc. of SPIE, Vol. 6113, San Jose, CA, Jan. 2006.
- [12] M. A. Helmbrecht, M. He, T. Juneau, M. Hart, N. P. Doble, "Segmented MEMS Deformable-Mirror for Wavefront Correction," Invited Presentation, Proc. of SPIE, Vol. 6376, Boston, MA, Oct. 2006.
- [13] R. G. Lyon and M. Clampin, "Space Telescope Sensitivity and Controls for Exoplanet Imaging", J. of Opt. Eng. 51(1), 2012
- [14] R. G. Lyon, M. Clampin, "Vacuum Nuller Testbed (VNT) Performance, Characterization and Null Control: Progress Report", Proc of SPIE 8151 (2011)
- [15] R. G. Lyon, M. Clampin, P. Petrone, U. Mallik, R. Mauk, "Telescopes in Near Space: Balloon Exoplanet Nulling Interferometer (BENI)", AAS, Austin TX, January (2012)
- [16] M. R. Bolcar, R. G. Lyon, "Approaches for Achieving Broadband Achromatic Phase Shifts for Visible Nulling Coronagraphy", Proc of SPIE 8445 (2012)